

Forced Near-Inertial Motion and Dissipation of Low-Frequency Kinetic Energy in a Wind-Driven Channel Flow

STEPHANNE TAYLOR AND DAVID STRAUB

Department of Atmospheric and Oceanic Science, McGill University, Montreal, Québec, Canada

(Manuscript received 25 March 2015, in final form 15 October 2015)

ABSTRACT

Using primitive equation simulations, a zonally periodic channel is considered. The channel flow is forced by a combination of steady and high-frequency winds. The high-frequency forcing excites near-inertial motion, and the focus is on how this influences the low-frequency, nearly geostrophic part of the flow. In particular, this study seeks to clarify how Reynolds stresses exerted by the near-inertial modes affect the low-frequency kinetic energy. In the system considered, the near-inertial Reynolds stresses (i) serve as a sink term in the low-frequency kinetic energy budget and (ii) transfer low-frequency kinetic energy downward from the mixed layer. Transfer spectra show the bulk of this sink to occur at relatively small horizontal wavenumber (i.e., in the mesoscale, not the submesoscale). The presence of near-inertial motion can also affect the kinetic-to-potential energy exchanges, especially within the low-frequency band.

1. Introduction

There has been considerable recent interest in the idea that balanced-to-unbalanced energy transfers and a subsequent forward cascade of unbalanced energy may play a significant role in the ocean's mechanical energy budget. Potential mechanisms for these transfers include interactions between geostrophic flow and rough topography (Nikurashin et al. 2012), spontaneous generation of unbalanced motion such as inertia-gravity waves (see, in particular, Molemaker et al. 2005; Molemaker and McWilliams 2010; Vanneste 2013), and wave capture (Bühler and McIntyre 2003, 2005). Work by Xie and Vanneste (2015) and by Gertz and Straub (2009) consider interaction between near-inertial and geostrophic modes but focus on regimes where the near-inertial motion is externally forced. Both find that this can result in an energy sink for the balanced flow.

Nikurashin et al. (2012) show that the generation of inertia-gravity waves in association with geostrophic flow over rough topography can provide a sink for geostrophic energy. This can be seen as a balanced-to-unbalanced transfer and likely plays a significant role in

the overall energetics of the balanced flow. Their simulations suggest that energy is transferred from the geostrophic flow to the wave field and then is further transferred forward toward dissipation scales. They report that about 20% of the small-scale dissipation occurs in the interior (i.e., far above the topography). This has implications not only for vertical mixing in the ocean's interior but also as a mechanism to dissipate energy from the wind-driven, nearly geostrophic circulation.

There is a much larger body of work examining the loss of balance and how carefully balanced flows decay (e.g., Molemaker et al. 2005; Molemaker and McWilliams 2010; Williams et al. 2008; Ngan et al. 2004, 2008; Zeitlin 2008; Vanneste 2013). The unbalanced portion of the flow in these studies arises either in association with a seeded instability (as in Molemaker et al. 2005; Williams et al. 2008) or through spontaneous generation of inertia-gravity waves (e.g., Zeitlin 2008; Danioux et al. 2012; Vanneste 2013, and references therein). While the exact mechanism for generating the unbalanced component of the flow varies, the presence of unbalanced motion implies a path to dissipation for the balanced flow. Typically, both the unbalanced flow and the related sink of balanced energy are weak. This is particularly true for low Rossby number flows, where growth rates of unbalanced motion are exponentially small (Vanneste 2008). Additionally, any generated unbalanced energy is readily cascaded forward, for

Corresponding author address: Stephanie Taylor, Department of Atmospheric and Oceanic Science, McGill University, 805 Sherbrooke St. W., Montreal, QC H3A 0B9, Canada.
E-mail: stephanne.taylor@mail.mcgill.ca

example, by a near-resonant wave–wave–vortex interaction, which has been shown by [Bartello \(1995\)](#) to be robust in the low Rossby number, low Froude number limit.

By contrast, the ocean is not carefully balanced: variable winds, storms, tides, and solar radiation all force the ocean on short time scales. There is some disagreement as to how much of the total wind work done on the ocean falls in the near-inertial band; estimates range from 0.3 to 1.4 TW, depending on the method of calculation and assumptions about the structure of the upper ocean (see [Alford 2001](#); [Watanabe and Hibiya 2002](#); [Alford 2003a](#); [Jiang et al. 2005](#); [Furuichi et al. 2008](#); [Rimac et al. 2013](#)). This is comparable to the 0.7–1.0 TW of wind work done on the geostrophic flow ([Wunsch 1998](#); [Huang et al. 2006](#); [Scott and Xu 2009](#); [Zhai et al. 2012](#)). The bulk of the total wind work done on the oceans occurs in the storm tracks over the Southern Ocean, the North Atlantic, and the North Pacific ([Wunsch 1998](#); [Scott and Xu 2009](#)). There is also a strong seasonality, with more near-inertial energy input in the winter months ([Furuichi et al. 2008](#); [Rimac 2014](#)).

Unlike much of the work on how precisely balanced flows decay, the wave capture framework ([Bühler and McIntyre 2003, 2005](#)) is unconcerned with the specific mechanism of generation of the wave packet. Rather, it presupposes that a wave packet exists and describes a situation in which it passes through the strain field generated by a vortex dipole. As the packet travels through the background strain field, it strongly refracts or even “freezes” in the vortex field. In refracting or freezing, the horizontal wavenumber of the packet increases, which in their framework implies an increase in wave energy. That is, for the pseudomomentum–impulse budget to be conserved, the wave energy increases and the dipole adjusts accordingly. This can be thought of as a balanced-to-unbalanced energy transfer in association with a forward cascade of unbalanced energy. Note that the wave capture framework assumes a clear separation of both temporal and spatial scales between the small, contained wave packet and the large vortex dipole.

Other recent work has focused on how near-inertial motion can exchange energy with geostrophic flow. [Xie and Vanneste \(2015\)](#) approach the problem of wave–mean interaction using a generalized Lagrangian mean (GLM) framework ([Soward and Roberts 2010](#); [Young and Ben Jelloul 1997](#)). Their framework does not assume a spatial-scale separation, instead only a frequency separation (i.e., near-inertial modes are superimposed on a geostrophic background flow). This leads to a system in which both total energy and near-inertial kinetic energy are separately conserved. Any increase in

near-inertial potential energy, then, must result from an implied balanced-to-unbalanced energy transfer. This suggests that strongly forced near-inertial motion can result in a sink of geostrophic energy.

Work by [Whitt and Thomas \(2015\)](#) and [Grisouard and Thomas \(2015\)](#) consider two other ways in which near-inertial motion can extract energy from geostrophic flow. Whitt and Thomas examine how lateral shear can mediate a transfer of energy from geostrophic to near-inertial flow in both linear and nonlinear simulations, whereas Grisouard and Thomas demonstrate that near-inertial waves reflecting off the ocean’s surface can extract energy from geostrophic flow via lateral buoyancy gradients. The mechanisms presented by [Xie and Vanneste \(2015\)](#), [Whitt and Thomas \(2015\)](#), and [Grisouard and Thomas \(2015\)](#) all require different restrictions on nondimensional parameters: [Xie and Vanneste \(2015\)](#) requires a small Rossby number, [Whitt and Thomas \(2015\)](#) uses $O(0.5\text{--}1)$ Rossby numbers, and [Grisouard and Thomas \(2015\)](#) characterizes the interaction with a Richardson number and a length scale for the energy flux. Together with the other mechanisms described above, these recent papers suggest that there may be several ways in which near-inertial waves can extract energy from balanced flow. All three of these recently proposed mechanisms appear to filter the near-inertial Reynolds stresses exerted on the geostrophic flow, which was the focus of [Gertz and Straub \(2009\)](#) and will be emphasized here.

[Gertz and Straub \(2009\)](#) also suggest that forced near-inertial motion can lead to a sink of geostrophic energy. They examine the wind-driven double-gyre problem in a midlatitude β -plane basin using a multilevel version of the unstratified hydrostatic equations. The vertical wavenumber $k_z = 0$ modes obey dynamics similar to the barotropic quasigeostrophic equations but with an additional term involving the $k_z \neq 0$ modes, which correspond to inertial oscillations in the linear limit. When the near-inertial modes are forced, they produce Reynolds stresses that can extract energy from the low-frequency ($k_z = 0$) modes. This sink can be substantial: if sufficient near-inertial wind forcing is applied, the bottom drag coefficient can be reduced to zero with the flow remaining in an oceanographically relevant regime ([Gertz and Straub 2009](#)). A key difference between the mechanism proposed by Gertz and Straub and that proposed by Xie and Vanneste is that the latter relies on the creation of unbalanced potential energy, whereas the former does not. Additionally, the mechanism described by Gertz and Straub requires the Rossby number to be $O(1)$ at least locally, while the Xie and Vanneste framework assumes an asymptotically small Rossby number.

Our motivation for the present paper was to revisit the mechanism proposed by Gertz and Straub but in a more realistic, stratified setting. We take a modeling approach and consider wind-driven simulations of the Parallel Ocean Program (POP; a primitive equation ocean circulation model) in a zonally reconnecting channel centered at high latitudes. The model is forced with a combination of steady and high-frequency (HF) winds. The former excites a nearly geostrophic flow, characterized by mesoscale eddies and quasi-zonal jets, while the latter adds near-inertial energy. Our goal is to examine how this near-inertial energy influences the low-frequency, nearly geostrophic, flow. In particular, we focus on a mechanism whereby Reynolds stresses associated with the high-frequency motion feed back onto the low frequencies. We will refer to this as an “advective sink” of geostrophic energy.

In [section 2](#), we give details of how our simulations are set up. [Section 3](#) presents the effect of adding near-inertial energy on the kinetic energy (KE) budget, and details of the advective sink, including vertical and horizontal structure, are presented in [section 4](#). We then discuss our results and draw some conclusions in [section 5](#).

2. Model and experimental design

We consider an eddy-permitting wind-driven flow in a spherical coordinate primitive equation channel setting. POP is configured as a 5.5-km-deep reentrant channel extending from 43° to 67°S and spanning 60° in longitude. Bottom topography takes the form of a meridionally aligned Gaussian ridge of height 1.8 km and decay scale of 7.5°. This allows for topographic form drag, which is needed to balance the zonal momentum budget in channel flows. The wind forcing includes two components: (i) a steady, zonally uniform eastward stress with a sinusoidal meridional profile peaked in the center of the channel and (ii) a spatially uniform zonal stress that oscillates at high frequencies. The former is meant to drive a nearly geostrophic eddy flow, while the latter primarily excites near-inertial motion; note that the wind stress has no meridional component at any frequency.

We use the McDougall, Wright, Jackett, and Feistel equation of state ([McDougall et al. 2003](#)) and initialize the model with the Levitus data for potential temperature $\theta(z)$ and salinity $s(z)$ ([Levitus and Isayev 1992](#)). The vertical grid has 20 levels, with thickness varying from 25 m at the surface to 400 m at depth. The horizontal resolution is 1/10°, which is about 11 km in the meridional direction and varies between 4.3 and 8.1 km in the

TABLE 1. Various model parameters and settings.

Model parameter	Parameter value
Zonal grid spacing	0.1°, 4.1–8.2 km
Meridional grid spacing	0.1°, 11.2 km
Vertical grid spacing	25–400 m
Time steps per day	500
Mixing interval	17
Coriolis parameter	$f_0 = 1.18 \times 10^{-4} \text{ s}^{-1}$ $f_{\min} = 0.99 \times 10^{-4} \text{ s}^{-1}$, $f_{\max} = 1.34 \times 10^{-4} \text{ s}^{-1}$
Quadratic bottom drag coefficient	2.5×10^{-3}
Horizontal biharmonic viscosity momentum coefficient	$-6.0 \times 10^{15} \text{ cm}^4 \text{ s}^{-1}$
Horizontal biharmonic viscosity tracer coefficient	$-2.0 \times 10^{15} \text{ cm}^4 \text{ s}^{-1}$
KPP upper background diffusivity	$0.250 \text{ cm}^2 \text{ s}^{-1}$
KPP lower background diffusivity	$0.025 \text{ cm}^2 \text{ s}^{-1}$
KPP transition depth	1700 m
KPP variation inverse length scale	0.0050 m^{-1}
Advection scheme	Third-order upwind
Gaussian ridge parameters	$x_0 = 30^\circ$, height = 1.8 km, $\sigma = 7.5^\circ$

zonal direction. This corresponds to eddy-permitting resolution, and submesoscale features are not resolved. Vertical mixing is handled with a KPP scheme ([Large et al. 1994](#)), and a biharmonic viscosity is used to remove small-scale momentum variance. A quadratic bottom drag with a unitless coefficient of 2.5×10^{-3} is also imposed. Details of the model setup are summarized in [Table 1](#).

We spin up the model for 100 yr using steady forcing only:

$$\tau_{\text{steady}} \equiv \tau_0 \{1 + \cos[2\pi(\theta - \theta_0)/\Delta\theta]\}, \quad (1)$$

where θ_0 is the center latitude, and $\Delta\theta \equiv \theta_{\text{north}} - \theta_{\text{south}}$. This gives a stress that goes to zero on the northern and southern edges of the channel and reaches its maximum τ_0 in the center. Three values of τ_0 are considered: 0.03, 0.15 and 0.30 N m^{-2} ; we call these the weak, median, and strong levels of steady forcing, respectively. The median level of forcing corresponds roughly to the observed zonally and temporally averaged stress at these latitudes ([Josey et al. 2002](#); [Huang et al. 2006](#); [Abernathey et al. 2011](#)).

We emphasize that although we use forcing values typical of the Southern Ocean to scale our steady wind stress, it is not our intent to model the Antarctic Circumpolar Current *per se*; rather, we aim to produce an eddy geostrophic flow in a generic but oceanographically relevant regime. Note that no buoyancy forcing is applied; this is done to ensure that any observed effects are primarily due to the addition of high-frequency winds, rather than a secondary interaction due to any interaction between forcings.

The combined steady and high-frequency forcing is thus $\tau_{\text{steady}}^x(y) + \tau_{\text{NI}}^x(t)$, where the latter is a spatially uniform zonal stress that we describe with a stationary stochastic function $\alpha(t)$. We define $\tau_{\text{NI}}^x(t) \equiv \tau_1 \alpha(t)$, where τ_1 is a constant and $\alpha(t)$ is peaked in the near-inertial (NI) band, as specified below. Because any small low-frequency tail could directly excite a low-frequency response, and our aim was to analyze how high-frequency forcing might indirectly affect the low-frequency flow, we specify $\alpha(t)$ in such a way that it contains high frequencies exclusively. We use a series of sinusoids with frequencies varying from $f_0/2$ to $2f_0$ modulated by a Gaussian envelope, that is,

$$\alpha(t) = \sum_{n=1}^N a(\omega_n) \sin(\omega_n t + \phi_n), \quad (2)$$

where $a(\omega_n) = N^{-0.5} \exp[-(\omega_n - f_0)^2/2\sigma^2]$; f_0 is the Coriolis frequency at the latitude in the middle of the channel; ϕ_n is a random phase; $\sigma = f_0/6$; and ω_n is linearly sampled from $f_0/2$ to $2f_0$ using a total of $N = 10000$ frequencies. A power spectrum of a typical $\alpha(t)$ is included in Fig. 2 (shown below).

This structure of $\alpha(t)$ results in a time series with an expected rms value of unity, and the explicit truncation ensures that there is no low-frequency component. The magnitude τ_1 of τ_{NI}^x is varied to produce different levels of the near-inertial response. Specifically, for each τ_0 , we consider five values of τ_1 , such that the ratio $\xi \equiv \tau_1/\tau_0$ takes on values of 0, 0.2, 0.35, 0.5, and 0.75. We emphasize that τ_{NI}^x has no spatial structure; it is simply an ad hoc forcing designed to add near-inertial motion to the system.

Following a 100-yr spinup of our control runs (i.e., using τ_{steady} only), ensembles of simulations are carried out with high-frequency forcing added. Each ensemble member was integrated for two years. A period of 320 days was used to allow for adjustment to the high-frequency forcing; we found this to be adequate by examining how quickly the bottom drag and viscosities responded to the additional forcing. The remaining 410 days were used for analysis. Ideally, one longer time series would be used for analysis; however, the analysis itself was memory intensive, and, for this reason, it was preferable to consider ensembles instead. Typically, 10 ensemble members were analyzed individually, and the resulting statistics were averaged. For consistency, we use the same set of 10 time series of $\alpha(t)$ to construct our high-frequency wind forcing for all values of τ_0 and ξ . For each 410-day ensemble member, time series of velocities (and other quantities) were saved at each grid point. Fourier methods were then used to decompose this data into low- and high-frequency components:

$\mathbf{u} = \mathbf{u}^< + \mathbf{u}^>$, where the superscripts $<$ and $>$ denote low- and high-pass filtering.

Throughout this paper, we use near inertial, high frequency, and (to a lesser extent) unbalanced to be equivalent; similarly, geostrophic, low frequency, and balanced are used interchangeably. Some calculations are difficult to do accurately using our low- and high-passed quantities; for these, we instead use a geostrophic–ageostrophic flow decomposition. We are relaxed with our language because we are not concerned with the exact nature of the balance; rather, our aim is to assess the extent to which forced near-inertial motion might influence the evolution of the underlying, essentially balanced flow.

3. Kinetic energy response

We consider simulations using all three base states ($\tau_0 = 0.03, 0.15, 0.30 \text{ N m}^{-2}$) following 100-yr spinups. Figure 1 shows four snapshots of surface speed from the median base state, with and without high-frequency forcing; snapshots from the strong and weak base states show similar behavior. Figure 1a shows the full speed of the control run toward the end of the 2-yr simulation; note that the most energetic region lies in the middle of the channel over and on the lee side of the ridge. Figure 1b is similar but with $\xi = 0.35$, while Figs. 1c and 1d show this same snapshot decomposed into low- and high-frequency components. Note that the near-inertial motion is distributed over the domain, while the low-frequency energy is concentrated in central latitudes. The near-inertial flow forms quasi-zonal bands that propagate equatorward; for example, the region of high kinetic energy currently visible in Fig. 1d near the southern edge of the domain will be displaced equatorward in subsequent snapshots. This propagation is a well understood phenomenon (see, particularly, Garrett 2001; Alford 2003b; Bühler 2003).

For the median base state, typical geostrophic surface speeds in the energetic region are $0.3\text{--}0.4 \text{ m s}^{-1}$, and the horizontally averaged speed ranges from about 0.15 m s^{-1} at the surface to half that in the abyss. Near-inertial velocities in the $\xi = 0.35$ ensemble have a maximum value around 0.40 m s^{-1} but typical values are closer to $0.10\text{--}0.15 \text{ m s}^{-1}$.

In all three base states, the deformation radius L_d varies with latitude, with smaller radii found at the poleward (southern) side of the channel. Values range from $9.5 \leq L_d \leq 15 \text{ km}$ for the strong base state, to $11 \leq L_d \leq 20 \text{ km}$ for the median base state, to $14.5 \leq L_d \leq 22 \text{ km}$ for the weak base state. As such, L_d is marginally resolved in all three base states, and these simulations should be viewed as “eddy permitting.” The average mixed

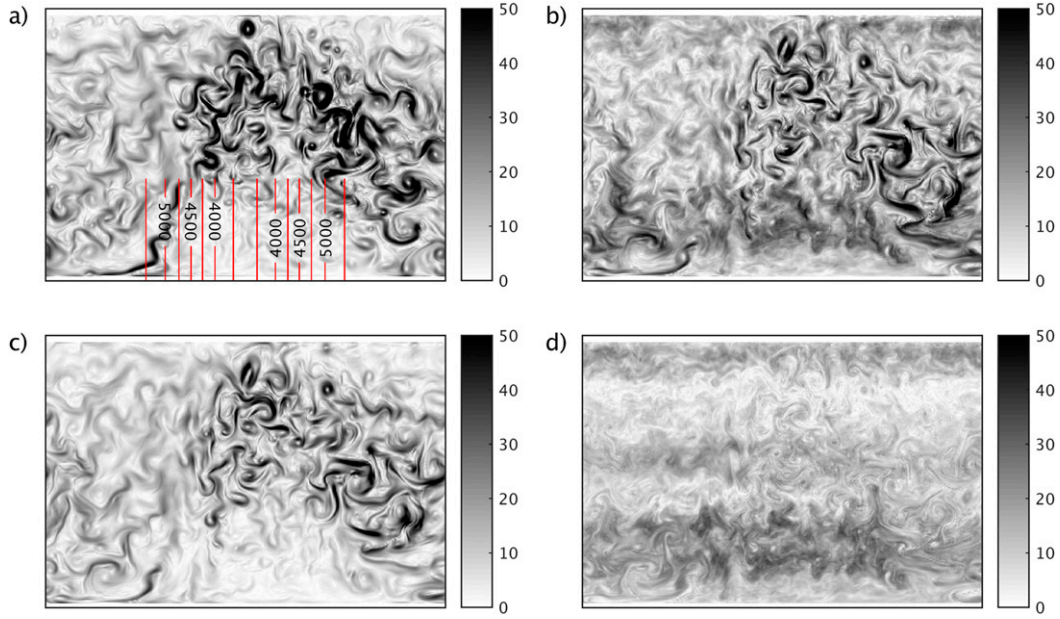


FIG. 1. Typical snapshots of the surface speed. The top row shows (a) the control run and (b) a $\xi = 0.35$ run. The bottom row splits the $\xi = 0.35$ snapshot into (c) low-frequency and (d) high-frequency speeds. All units are cm s^{-1} . Panel (a) also shows partial topographic contours; contours extend the breadth of the channel but are shown only at the bottom edge to avoid obscuring the energetic flow. The channel spans 60° longitude and 24° latitude.

layer depth generated by the median steady wind stress is about 350 m, consistent with observed wintertime values over portions of the Southern Ocean (Dong et al. 2008).

a. Balanced kinetic energy

Figure 2 shows the frequency power spectra for kinetic energy of the median base state ensembles at the surface and a power spectrum of a typical τ_1 . Frequency is scaled so that $\omega = 1$ corresponds to a period of 2 days. High-frequency energy is negligible in the base state and increases markedly in response to the high-frequency forcing. While the near-inertial response is strongest near the surface, it is also present throughout the water column. For $\omega \geq 1$, the $\xi > 0$ ensembles show a substantial increase in high-frequency energy compared to the control run, and there is a clear spectral gap between $\omega = 1$ and $\omega = 2$. We choose $\omega = 1$ to be the threshold between low and high frequencies, as it is at this point that the high-frequency motion starts to diverge in behavior from the control run. Our results are not sensitive to this precise choice of cutoff, so long as the cutoff lies in the spectral gap.

The near-inertial response to τ_{NI}^x is clear in Fig. 2, but the logarithmic scale obscures what changes, if any, occur in the low-frequency band. This is clarified in Fig. 3, which shows vertical profiles of horizontally integrated low- and high-passed kinetic energy as a function of depth for the five values of ξ and all three base states.

For clarity, the data for the low-frequency kinetic energy in the top 200 m are shown in insets.

There is a clear tendency for the low-frequency (and barotropic) kinetic energy to decrease with increasing ξ for the strong and median base states. This reduction is modest for $\xi = 0.2$ but becomes significant for larger

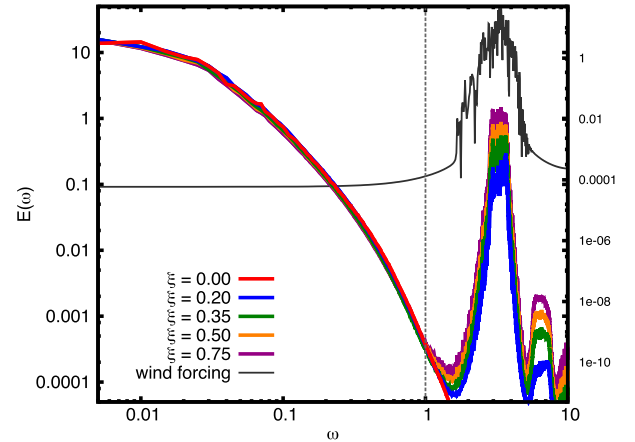


FIG. 2. Ensemble averages of the $\tau_0 = 0.15 \text{ N m}^{-2}$ kinetic energy frequency spectra at the surface. A typical power spectrum of τ_1 , the high-frequency wind forcing, is also shown for comparison. The line delineating the low-frequency and near-inertial band is $\omega = 1$ and is shown with a dashed line. The frequency ω is normalized such that $\omega = 1$ corresponds to a time period of 2 days. The y axis on the right is for the wind forcing.

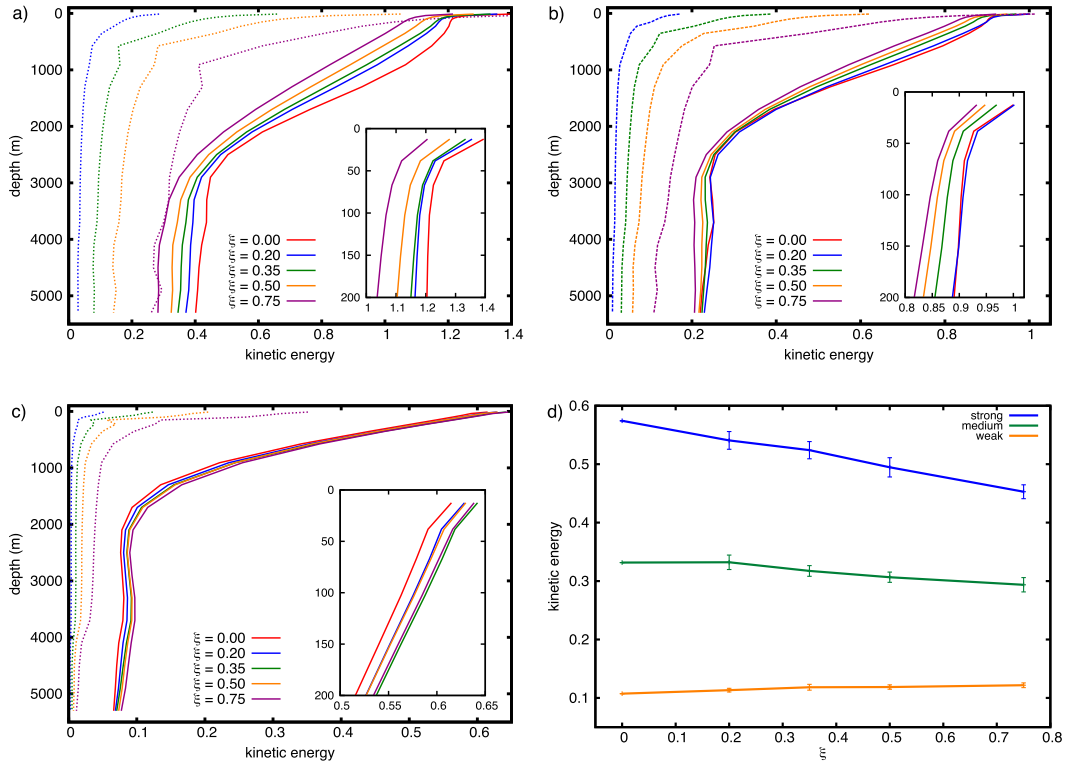


FIG. 3. Depth profiles of the low- (solid) and high-frequency (dashed) kinetic energy for (a) strong, (b) medium, and (c) weak base state ensembles. Insets show the low-frequency data for the top 200 m. (d) The low-frequency barotropic kinetic energy for all three base states as a function of near-inertial forcing. Normalization for all panels is such that the value of the control run of the medium base state at the surface is 1.0. The ratio τ_1/τ_0 is denoted as ξ , and indicates the amount of near-inertial forcing added to the system.

values of ξ . By contrast, increased ξ corresponds to an increase of $KE^<$ in the weak base state ensembles. This increase is relatively small—note the tight clumping of profiles in Fig. 3c—and appears to lessen at larger values of ξ . The changes are seen at all depths, although they are largest in the upper ocean.

The high-frequency kinetic energy is also strongly concentrated in the upper ocean and drops off sharply at the base of the mixed layer. A small, depth-independent amount of near-inertial kinetic energy is found in the abyss. This is consistent with previous work showing that eddies can efficiently channel near-inertial energy from the surface into the lower ocean (Zhai et al. 2005).

b. Kinetic energy budgets

Table 2 shows a kinetic energy budget for the full flow in the median base state ensembles. In the control run, bottom drag damps 59% of the wind power input, vertical viscosity damps another 24% (mainly in the surface Ekman layer), and pressure work transfers the remaining 17% to potential energy. The steady wind input does not vary significantly with ξ , while the high-frequency power input increases roughly quadratically with τ_1 and

is dissipated primarily by vertical viscosity. Dissipation by bottom drag and transfer to potential energy by pressure work also tend to increase with ξ , though the change in the pressure work is not monotonic.

The residual shown in Table 2 increases in magnitude from 1% in the control run to 29% in the $\xi = 0.75$ ensemble; however, its statistical error is comparable to its magnitude at all values of ξ . This persistent trend is principally due to the pressure work term. POP has an emphatically recommended option to average the pressure gradient between time steps. The pressure work diagnostic, however, is extremely sensitive to small changes in the quantities used to calculate $\mathbf{u} \cdot \nabla P$, and this sensitivity is exacerbated by the addition of the high-frequency forcing. Using pressure averaging introduces an error into the calculation of the pressure work diagnostic, and this error increases with ξ . We emphasize that this is an issue with the calculation of the diagnostics and not with the integration of the flow. Increasing the temporal resolution reduces the residual in the kinetic energy budget; details are presented in appendix A.

Table 3 details a summary of the overall balanced KE budget for the median base state ensembles. As

TABLE 2. Domain-integrated sources and sinks of the kinetic energy budget for the full flow with $\tau_0 = 0.15 \text{ N m}^{-2}$. NI KE/KE indicates the fraction of the total kinetic energy that falls in the near-inertial band.

Term	Control	$\xi = 0.20$	$\xi = 0.35$	$\xi = 0.50$	$\xi = 0.75$
NI KE/KE	0.00	0.06	0.14	0.23	0.36
Steady wind	1.00	0.98 ± 0.01	0.98 ± 0.01	0.97 ± 0.01	0.97 ± 0.01
HF wind	0.00	0.44 ± 0.02	1.21 ± 0.06	2.25 ± 0.12	4.48 ± 0.21
Bottom drag	-0.59	-0.63 ± 0.03	-0.65 ± 0.02	-0.72 ± 0.03	-0.87 ± 0.02
Pressure work	-0.17	-0.16 ± 0.03	-0.23 ± 0.03	-0.29 ± 0.02	-0.39 ± 0.03
Horizontal viscosity	-0.01	-0.03 ± 0.001	-0.05 ± 0.002	-0.06 ± 0.002	-0.08 ± 0.001
Vertical viscosity	-0.24	-0.57 ± 0.01	-1.17 ± 0.04	-2.00 ± 0.09	-3.82 ± 0.16
Residual	0.01	0.03 ± 0.05	0.09 ± 0.08	0.15 ± 0.15	0.29 ± 0.26

mentioned previously, for some terms it is more convenient to use the geostrophic velocity as a proxy for the low-frequency velocity. Specifically, we use the geostrophic velocity for the wind input, bottom drag, and horizontal and vertical viscosity diagnostics, and the other diagnostics are calculated with low-frequency velocities. For all ensembles, about 75% of the energy input by steady winds is pumped into the geostrophic flow. The remaining 25% feeds an Ekman-like component of the low-frequency flow; this is damped primarily by vertical viscosity and not further considered. As ξ increases, bottom drag removes significantly less kinetic energy from the system. Pressure work also removes slightly less energy with increasing ξ , though it does not show as clear a trend as the bottom drag does. Horizontal viscosity increases with ξ but is insufficient to offset the changes in bottom drag and pressure work. The vertical viscosity acting on the geostrophic velocity is small for all values of ξ . To close the kinetic energy budget, then, a term associated with the Reynolds stresses exerted by the near-inertial motion on the low-frequency motion is required. The term is labeled an advective sink in Table 3; we define and discuss this term in detail in the next section.

Partial kinetic energy budgets for the strong and weak base state ensembles are shown in Table 4. The strong ensembles show trends similar to those in Table 3. Bottom drag decreases and the advective sink increases with increasing ξ . The pressure work diagnostic behaves more erratically, first increasing in magnitude slightly and then decreasing. By contrast, the weak ensembles show a different behavior. As ξ increases, the advective sink behaves much as it does in other ensembles, but bottom drag removes more energy from the system. Additionally, pressure work converts less kinetic energy to potential energy, and at large values of ξ it even changes sign, that is, it provides a source of kinetic energy. This change in pressure work results in the increase in low-frequency kinetic energy seen in Fig. 3c.

All three budgets illustrate that the addition of near-inertial motion has two broad effects: it induces an advective sink, which dissipates 2%–14% of the balanced

kinetic energy pumped in by the steady winds, and it induces changes in the existing sinks of low-frequency KE. Bottom drag shows a variable response depending on the base state, while the horizontal viscosity consistently removes more energy with ξ . Pressure work has a variable response, and the relative importance of the pressure work term varies between the three sets of ensembles. In the absence of near-inertial motion, pressure work removes about 6% of the balanced KE of the strong base state, but this jumps to a full 30% for the weak base state. Moreover, in the weak base state ensembles, the pressure work shows a stark positive trend that is largely absent in the median and strong ensembles. As such, changes in the pressure work term have a larger impact on the weak base state ensembles than on either the median or strong ensembles.

4. The advective sink

This study was motivated by the suggestion (Gertz and Straub 2009) that near-inertial motion might interact significantly with the low-frequency part of the flow. Advection of near-inertial momentum by the near-inertial velocity field contains a low-frequency component, and this appears in the low-passed horizontal momentum equation. To calculate the interaction, we first form the low- and high-frequency energy equations and isolate the advection terms:

$$\frac{\partial \text{KE}^<}{\partial t} = -\mathbf{u}^< \cdot (\mathbf{v}^< \cdot \nabla) \mathbf{u}^< - \mathbf{u}^< \cdot [(\mathbf{v}^> \cdot \nabla) \mathbf{u}^>]^< + \dots, \quad (3)$$

and

$$\begin{aligned} \frac{\partial \text{KE}^>}{\partial t} = & -\mathbf{u}^> \cdot (\mathbf{v}^< \cdot \nabla) \mathbf{u}^> - \mathbf{u}^> \cdot (\mathbf{v}^> \cdot \nabla) \mathbf{u}^< \\ & - \mathbf{u}^> \cdot [(\mathbf{v}^> \cdot \nabla) \mathbf{u}^>]^> + \dots. \end{aligned} \quad (4)$$

Here, \mathbf{u} is the horizontal velocity, and $\mathbf{v} = \mathbf{u} + \hat{\mathbf{z}}w$. We focus on the second term on the right-hand side of (3), as this is the term that allows the high-frequency motion to

TABLE 3. Domain-integrated sources and sinks of the kinetic energy budget for the balanced flow with $\tau_0 = 0.15 \text{ N m}^{-2}$. Wind, drag, and viscous terms are calculated using the geostrophic flow; pressure and advective terms are calculated using the low-frequency velocity. Comparison with Table 2 shows that input by the steady winds to the geostrophic flow is only 74% of the total; the remaining 26% feeds an Ekman-like flow, which is dissipated by vertical viscosity. Wind input from high-frequency winds is small and so not listed.

Term	Control	$\xi = 0.20$	$\xi = 0.35$	$\xi = 0.50$	$\xi = 0.75$
Steady wind	0.74	0.74 ± 0.01	0.75 ± 0.01	0.75 ± 0.01	0.76 ± 0.01
Bottom drag	-0.52	-0.52 ± 0.02	-0.46 ± 0.02	-0.44 ± 0.02	-0.40 ± 0.02
Pressure work	-0.18	-0.14 ± 0.01	-0.16 ± 0.03	-0.16 ± 0.01	-0.10 ± 0.02
Advective sink	0.00	-0.02 ± 0.001	-0.05 ± 0.002	-0.08 ± 0.002	-0.14 ± 0.01
Horizontal viscosity	-0.01	-0.03 ± 0.0006	-0.05 ± 0.002	-0.06 ± 0.002	-0.08 ± 0.001
Vertical viscosity	-0.01	-0.01 ± 0.0001	-0.01 ± 0.0003	-0.02 ± 0.0004	-0.03 ± 0.01
Residual	0.02	0.02 ± 0.03	0.02 ± 0.04	-0.01 ± 0.03	0.01 ± 0.04

feed back onto the low-frequency flow. We call this term the advective sink or χ . To be consistent with model numerics, χ is calculated in flux form:

$$\begin{aligned} \chi &= -\mathbf{u}^< \cdot [\nabla \cdot (\mathbf{v}^> \mathbf{u}^>)]^< \\ &= -u^< [\nabla \cdot (\mathbf{v}^> u^>)]^< - v^< [\nabla \cdot (\mathbf{v}^> v^>)]^<. \end{aligned} \quad (5)$$

It will be convenient to split χ into horizontal and vertical components:

$$\begin{aligned} \chi &= \chi_H + \chi_V = -\mathbf{u}^< \cdot [\nabla \cdot (\mathbf{u}^> \mathbf{u}^>)]^< \\ &\quad - \mathbf{u}^< \cdot (w^> \mathbf{u}^>)_z^<. \end{aligned} \quad (6)$$

This decomposition isolates the contribution of increased vertical motion as a result of the near-inertial forcing to χ .

The domain-integrated values for the advective sink presented in Tables 3 and 4 were obtained by calculating χ at each point in space, integrating over the fluid, and averaging over the time and ensemble member. The tables show that χ is most significant (as a portion of the total balanced KE budget) when both the geostrophic and near-inertial parts of the flow are strong. Comparing χ to our estimate of the bottom drag acting on the geostrophic flow shows that the advective sink removes about 38% as much kinetic energy as does bottom drag for the $\tau_0 = 0.30 \text{ N m}^{-2}$ and $\xi = 0.75$ ensemble. This proportion varies with both base state and ξ . For example, it drops to 4.5% for the $\tau_0 = 0.30 \text{ N m}^{-2}$ and $\xi = 0.20$ ensemble and to 13% for the $\tau_0 = 0.03 \text{ N m}^{-2}$ and $\xi = 0.75$ ensemble.

While we focus on χ in this paper, we note that the second term on the right-hand side of (4) is that equation's counterpart to χ . Kinetic energy that χ extracts from the balanced flow is pumped into the high-frequency motion by $\chi_{\text{HF}} = \mathbf{u}^> \cdot (\mathbf{v}^> \cdot \nabla) \mathbf{u}^<$. Indeed, calculations show the volume integrals of χ and χ_{HF} to balance to within 2%–3% for our data. M. Claret (2015, personal communication) focuses on χ_{HF} in her work,

examining how trapped near-inertial waves interact with a strong front. Consistent with our observations, she finds that wave triad interactions extract energy from the background flow in favor of the near-inertial waves.

a. Vertical structure

Figure 4 plots vertical profiles of the horizontally integrated and time-averaged advective sink for all three base states. A strong surface intensification is seen in all three base states. More specifically, χ is substantial and negative in the upper ocean and switches signs below the mixed layer. This is related to χ_V , which is large compared to χ_H in the upper ocean. To leading order, then, χ_V transfers energy downward from the upper ocean, deepening the mixed layer. Nonetheless, integrating χ_V vertically results in a net sink of balanced kinetic energy. That is, the energy removed from the near-surface layers and not deposited (to the balanced flow) below is transferred to the high-frequency band.

By contrast, χ_H is negative or very weakly positive at all depths. As such, it serves primarily to remove low-frequency kinetic energy from the system rather than to redistribute it within the system. When integrated vertically, χ_H contributes 20%–50% of the total integrated value of χ . The proportion depends on both τ_0 and ξ : The value χ_H/χ is largest when both τ_0 and ξ are small, that is, when there is less vertical motion induced by the near-inertial forcing. The importance of χ_V was unexpected; previous results from Gertz and Straub (2009) found this term to play a minimal role. We do not have a wholly satisfying explanation of why the vertical component of χ is dominant in our system, and the dependence of the advective sink on the vertical structure of the fluid merits further investigation. We note that while the local values of the advective sink are dominated by χ_V , integrating χ_V and χ_H vertically results in values of comparable

TABLE 4. As in Table 3, but with $\tau_0 = 0.30 \text{ N m}^{-2}$ and $\tau_0 = 0.03 \text{ N m}^{-2}$. Values in this table are normalized such that the steady wind input into each ensembles' control run is 1.00. As before, the steady wind pumps energy into both the geostrophic and Ekman flows; the Ekman flow is dissipated by vertical viscosity near the surface and is not further considered. Note that the strong ensembles show a much stronger Ekman flow than the weak ensembles. Horizontal and vertical viscosities behave similarly to Table 3 for both sets of ensembles and are not shown.

	Term	Control	$\xi = 0.20$	$\xi = 0.35$	$\xi = 0.50$	$\xi = 0.75$
Strong ensembles	Steady wind	0.58	0.60 ± 0.01	0.61 ± 0.01	0.61 ± 0.01	0.62 ± 0.01
	Bottom drag	-0.46	-0.41 ± 0.01	-0.38 ± 0.01	-0.36 ± 0.02	-0.32 ± 0.02
	Advective sink	0.00	-0.02 ± 0.001	-0.04 ± 0.003	-0.07 ± 0.001	-0.12 ± 0.006
	Pressure work	-0.06	-0.11 ± 0.03	-0.10 ± 0.02	-0.09 ± 0.03	-0.05 ± 0.03
Weak ensembles	Steady wind	0.94	0.93 ± 0.01	0.93 ± 0.01	0.94 ± 0.01	0.93 ± 0.01
	Bottom drag	-0.53	-0.60 ± 0.02	-0.66 ± 0.03	-0.68 ± 0.04	-0.74 ± 0.07
	Advective sink	0.00	-0.02 ± 0.001	-0.04 ± 0.002	-0.06 ± 0.002	-0.10 ± 0.01
	Pressure work	-0.30	-0.19 ± 0.02	-0.14 ± 0.05	0.04 ± 0.07	0.23 ± 0.10

magnitude, and thus the net effect is a result of more equitable combination of both χ_V and χ_H than Fig. 4 may indicate.

b. Horizontal structure

To determine which horizontal scales contribute to χ , we calculate the horizontal transfer spectra $T(\kappa) = \text{Re}(A \cdot B^*)$ as a function of the one-dimensional horizontal wavenumber κ , where $*$ indicates a complex conjugate. Using $F(\cdot)$ to denote a two-dimensional horizontal Fourier transform, we define A and B by $A \equiv F(\mathbf{u}^<)$ and $B \equiv F[\nabla \cdot (\mathbf{v}^> \mathbf{u}^<)]$. We calculate the scalar product in Fourier space and bin the data according to wavenumber. Our use of spherical coordinates, however, makes the definition of κ somewhat complicated since the maximum and Nyquist zonal wavelengths are both functions of latitude. To ensure that a particular value of κ corresponds as closely as possible to a consistent length scale, we split the Fourier transform into three parts: First, we perform a one-dimensional FFT at each latitude in the zonal direction. We then reorganize the partially transformed data so that all data in one zonal bin corresponds to a single physical length scale, and finally we perform a meridional one-dimensional FFT. Details of this method, as well as sensitivity of our results to this manipulation, are given in appendix B.

Transfer spectra for χ at the surface and for all three base states are shown in Fig. 5. Also shown are transfer spectra at selected vertical levels for the $\tau_0 = 0.15 \text{ N m}^{-2}$ and $\xi = 0.5$ ensemble. The form of the spectra for the various base states and values of ξ is remarkably consistent; the results are distinguishable only by scale. For the surface and upper ocean, results show a robust sink between about $\kappa = 10$ and $\kappa = 100$ (corresponding to wavelengths ranging from ~ 50 to 500 km). The largest sink is at about $\kappa \sim 20$. In other words, the advective sink is a mesoscale, not a submesoscale, effect. We also note that the shape of the surface spectra at low-to-medium

wavenumbers is broadly similar to the shape of the 2D-to-3D transfer spectra in Gertz and Straub (2009); data from both studies show a peak in mesoscale wavenumbers. Unlike Gertz and Straub (2009), however, we do not see a positive peak at high wavenumbers.

Figure 5d shows results at selected vertical levels for the $\tau_0 = 0.15 \text{ N m}^{-2}$ and $\xi = 0.5$ ensemble. The shape of the transfer spectra throughout the mixed layer is similar, with peaks consistently near $\kappa \sim 20$. Deeper down, where $\chi > 0$, the transfer spectra have a similar shape but with the sign reversed. In the abyss, the transfer spectra are noisy, flatter, and slightly positive.

5. Discussion

We have found that adding a high-frequency wind forcing to an otherwise nearly geostrophic wind-driven channel flow results in a sink of low-frequency kinetic energy, that is, the near-inertial motion exerts Reynolds stresses that extract energy from the low-frequency flow. Our calculations show this sink to be present over a range of amplitudes for both the high- and low-frequency forcing. For the range of parameters considered, it dissipates between 2% and 14% of the energy input by the steady winds. Because a substantial fraction of the energy input by the steady winds is dissipated in the Ekman layer, this corresponds to χ dissipating 3%–38% as much as is dissipated by (the geostrophic) bottom drag. Larger fractions generally correspond to larger values of τ_0 and ξ . The horizontal and vertical structure of the sink is consistent across the range of parameters considered, and the domain-integrated value is sign definite (i.e., it is a consistent net sink) for all values of ξ and all three base states. For two of our base states, a reduction in low-frequency kinetic energy results. In our weakly forced base state, however, a slight increase in balanced kinetic energy is seen, even though χ remains a net sink. This appears to be related to

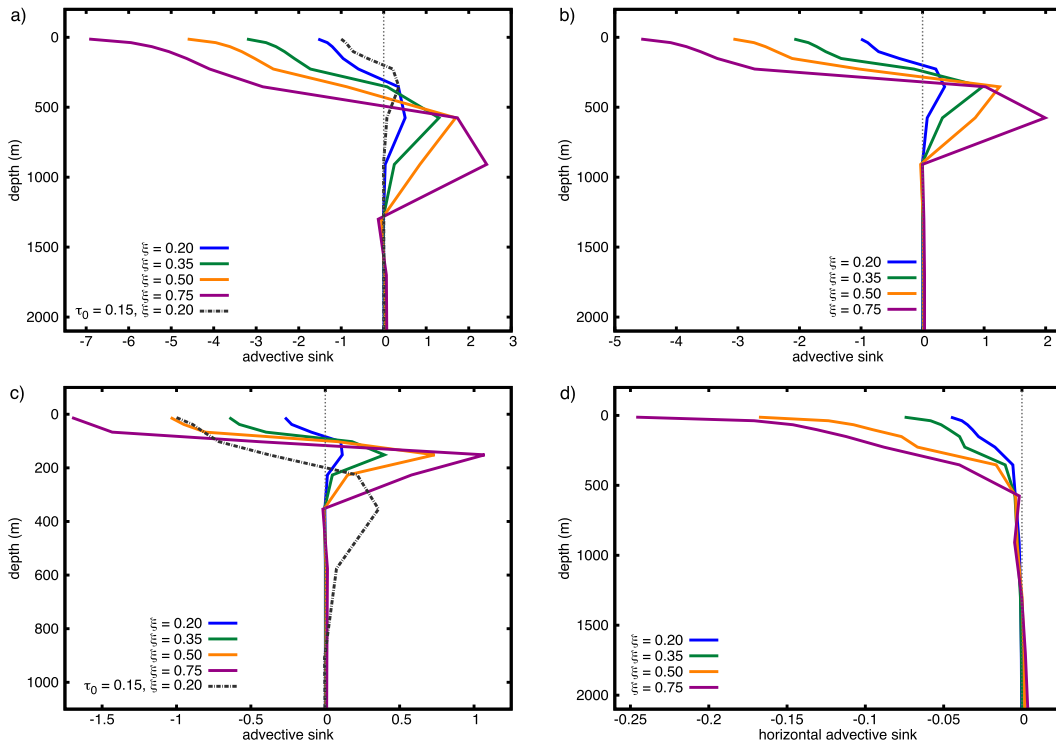


FIG. 4. Partial vertical profiles of the advective sink for the (a) strong, (b) medium, and (c) weak base states; note that the stronger the steady forcing, the deeper advective sink as a substantial (local) value. (d) The horizontal component χ_H for the median base state ensembles. All profiles are normalized such that the surface value of the $\tau_0 = 0.15 \text{ N m}^{-2}$ and $\xi = 0.20$ profile equals 1. Values in the abyss are small for all ensembles.

transfers between low-frequency kinetic and potential energy associated with the pressure work term.

In addition to changes in the low-frequency kinetic energy budget, near-inertial forcing also induces a deepening of the mixed layer and a small increase in zonal transport. The former is related to mixing brought about as the near-inertial modes lead to an increased shear at the base of the mixed layer. The latter is modest; zonal transport increases by about 6% in our $\xi = 0.5$ ensembles and less than 1.5% in our $\xi = 0.1$ ensembles. The increase is small, but the result is consistent across the range of parameters considered.

The bulk of the advective sink lies in the upper ocean, and it is important to note that our model does not contain the richness of dynamics known to be present there and often emphasized in other work (see, e.g., Fox-Kemper et al. 2008; Capet et al. 2008; Klein and Lapeyre 2009). Notably, we omit radiative and buoyancy forcing; this was a deliberate choice motivated by a desire to isolate the effect of adding the high-frequency winds. Given that χ is strongly dominated by the vertical contribution, some exploration of the advective sink using a system with rich mixed layer dynamics may be illuminating. Additionally, our resolution is modest, and the submesoscale is not well resolved. We emphasize,

though, that the transfer spectra of χ show that the dominant horizontal wavenumbers associated with χ are well resolved (see Fig. 5). The advective sink appears to be a mesoscale, not a submesoscale, phenomenon. Our choice of resolution was also related to computational constraints; the analysis required processing high-resolution time series of data for the entire domain, and we did not have the resources to do this at submesoscale-resolving resolution.

It is clear from our results that examining the effect of near-inertial motion on low-frequency kinetic energy is only part of the picture: the additional forcing has an impact on both the kinetic and potential energy of the system. While the kinetic response is remarkably consistent across the three base states examined, the response of the pressure work term varies substantially. Figure 6 shows the data for the pressure work and advective sink terms listed in Tables 3 and 4 and adds three single-run data points for the advective sink at low levels of near-inertial forcing ($\xi = 0.01, 0.05, 0.10$). The pressure work data for the weak ensembles show a starkly different trend than either the median or strong ensemble data, and further work will be required to fully understand why this is the case. For $\xi \geq 0.1$, the advective sink shows a linear dependence on ξ for all three

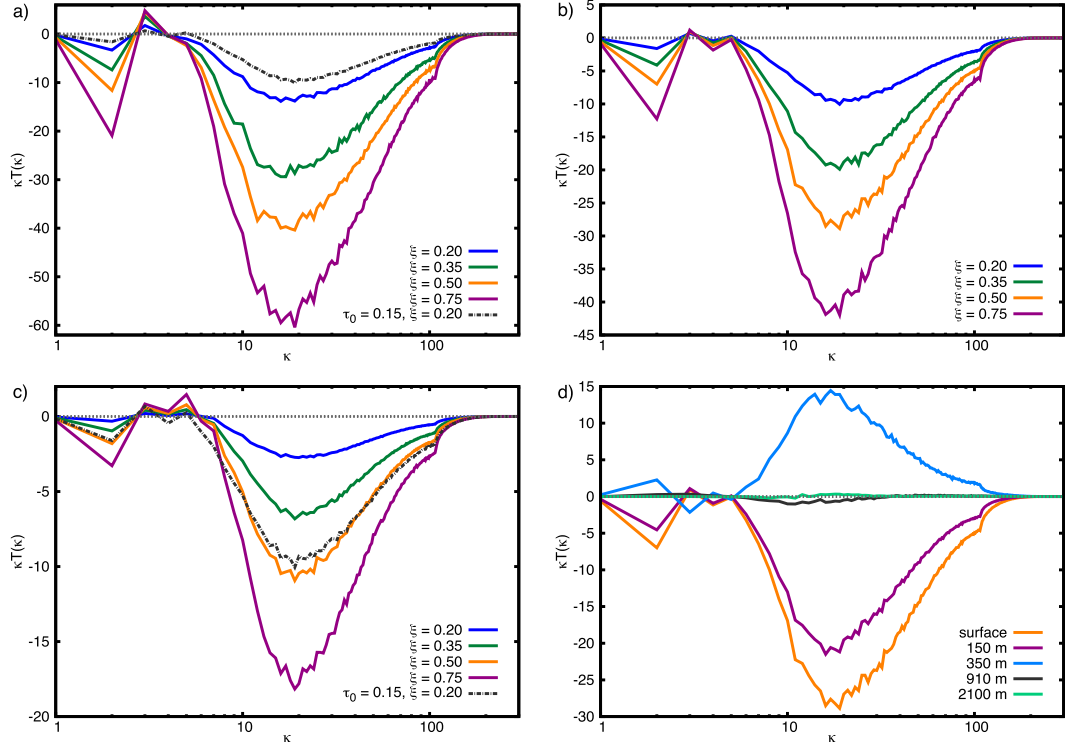


FIG. 5. The horizontal transfer spectra of the advective sink. The spectra at the surface for the (a) strong, (b) medium, and (c) weak base states respectively as a function of ξ . (d) Spectra at selected vertical levels for the $\tau_0 = 0.15 \text{ N m}^{-2}$ and $\xi = 0.50$ ensemble.

base states. Additionally, the data points with low values of ξ show that χ is robustly a sink even at very low levels of forcing (the $\tau_0 = 0.30 \text{ N m}^{-2}$ and $\xi = 0.01$ run contains $<0.15\%$ near-inertial KE in the surface layer). We find it interesting that even these minute levels of near-inertial energy induce a small advective sink near the surface.

The suggestion that forced near-inertial motion can lead to dissipation of balanced energy has also been a focus of recent work by [Xie and Vanneste \(2015\)](#). They consider a limit in which the geostrophic velocity is small compared to the near-inertial velocity. In our setting, this would correspond to a low value of τ_0 and a high value of ξ . More importantly, their dynamics are constrained by the assumption of a small Rossby number, whereas the Rossby number in our base state simulations can be locally $O(1)$.

The system they consider conserves both total energy and near-inertial kinetic energy. As such, any increase in near-inertial PE implies a corresponding reduction of balanced energy (see their section 5). In our model, the potential energy budget is complicated by a choice made early on in this study to use a two-component nonlinear equation of state. In a simpler setting (i.e., for a single constituent linear equation of state and assuming a

background stratification given by N^2), the buoyancy equation can be written as

$$\frac{\partial(b^{<} + b^{>})}{\partial t} + (\mathbf{v}^{<} + \mathbf{v}^{>}) \cdot \nabla(b^{<} + b^{>}) + (w^{<} + w^{>})N^2 = 0, \quad (7)$$

where forcing and dissipation terms are ignored. The potential energy equation is formed by multiplying (7) by $(b^{<} + b^{>})/N^2$; splitting this into low- and high-passed components gives

$$\frac{\partial \text{PE}^{<}}{\partial t} + \frac{b^{<}}{N^2} \mathbf{v}^{<} \cdot \nabla b^{<} = -\frac{b^{<}}{N^2} (\mathbf{v}^{>} \cdot \nabla b^{>})^{<} - w^{<} b^{<}, \quad (8)$$

and

$$\begin{aligned} \frac{\partial \text{PE}^{>}}{\partial t} + \frac{b^{>}}{N^2} \mathbf{v}^{<} \cdot \nabla b^{>} \\ = -\frac{b^{>}}{N^2} \mathbf{v}^{>} \cdot \nabla b^{<} - \frac{b^{>}}{N^2} (\mathbf{v}^{>} \cdot \nabla b^{>})^{>} - w^{>} b^{>}. \end{aligned} \quad (9)$$

At statistical equilibrium, the time derivative terms integrate to zero. The second term on the right-hand side

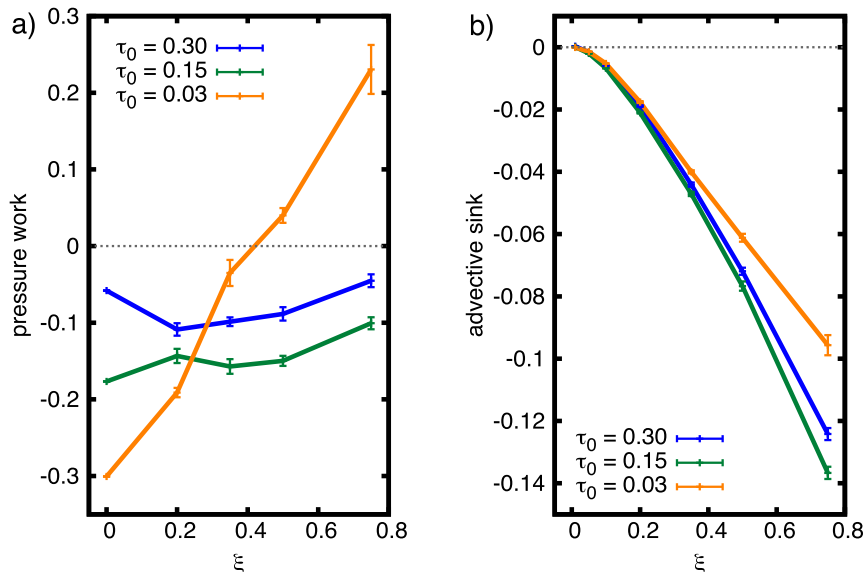


FIG. 6. (left) Pressure work and (right) advective sink vs ξ for all three values of τ_0 . Note that the pressure work term behaves more erratically and with larger statistical error than the advective sink. Note also that the pressure work term shows a significant positive slope for the weak base state ensembles.

of (9) involves high-frequency terms only and thus is not directly related to balanced-to-unbalanced transfer. In the Xie and Vanneste framework, an increase in $PE^>$ implies a decrease in the total balanced (or low frequency) energy. The first term on the right-hand side of (9) has an analog in (8); taken together, these two terms describe transfers between low- and high-frequency potential energy. That is, they appear analogous to χ and χ_{HF} in the kinetic energy equations. It thus seems possible that this transfer is related to that implied by the Xie and Vanneste mechanism.

Although there is a qualitative resemblance to χ , the two mechanisms are distinct. In fact, the advective sink we considered appears to be filtered in the Xie and Vanneste model, which is consistent with their assumption of a low base state Rossby number. In general, balanced-to-unbalanced energy transfers will include both interactions.

It is clear, particularly from recent work (Xie and Vanneste 2015; Whitt and Thomas 2015; Grisouard and Thomas 2015; M. Claret 2015, personal communication) that there are a variety of mechanisms by which near-inertial motion can extract energy from balanced flow. As such, there are two branches of inquiry that we are continuing to explore. One is to clarify the impact of near-inertial forcing on the potential energy budget. This includes further consideration of exchanges between the kinetic and potential energy as well as exchanges between the low- and high-frequency pools of potential energy, such as seems to be implied by Xie and

Vanneste (2015). The second is to use a more realistic prescription of the near-inertial wind forcing and to investigate how spatial and temporal intermittency of the winds affects the advective sink. Although it is not yet clear how important these routes to dissipation of balanced energy will prove to be globally, the idea that forced near-inertial motion can extract energy from the ocean's mesoscale clearly merits further investigation.

Acknowledgments. We thank Jin-Han Xie and Jacques Vanneste for their helpful and illuminating comments. We also thank the two reviewers for their thoughtful questions and comments. This work was supported by funding from NSERC. Computational resources were supplied by CLUMEQ and Compute Canada.

APPENDIX A

Details of Kinetic Energy Diagnostics

Since the pressure work diagnostic is sensitive to the size of the time step, we calculate the energy budget for $\tau_0 = 0.15 \text{ N m}^{-2}$ and $\xi = 0.5$ using three different time steps (see Table A1). Using 250 time steps a day results in a 27% residual, using 500 time steps a day results in a 15% residual, and using 1000 time steps a day reduces the residual to 8%. The model sensitivity to temporal resolution is mainly due to the pressure work and bottom drag terms. Both increase in magnitude with smaller

TABLE A1. Comparison of $\xi = 0.50$ and $\tau_0 = 0.15 \text{ N m}^{-2}$ ensembles simulated with three temporal resolutions. Note that the pressure work, and to a lesser extent the bottom drag, is sensitive to the change in time step.

Term	250 steps day^{-1}	500 steps day^{-1}	1000 steps day^{-1}
Steady wind	0.97 ± 0.005	0.97 ± 0.004	0.97 ± 0.001
HF wind	2.23 ± 0.10	2.25 ± 0.10	2.38 ± 0.12
Bottom drag	-0.68 ± 0.02	-0.72 ± 0.03	-0.75 ± 0.03
Pressure work	-0.25 ± 0.03	-0.29 ± 0.02	-0.32 ± 0.04
Horizontal viscosity	-0.05 ± 0.002	-0.06 ± 0.002	-0.07 ± 0.003
Vertical viscosity	-1.97 ± 0.07	-2.00 ± 0.08	-2.04 ± 0.09
Residual	0.26 ± 0.13	0.15 ± 0.15	0.08 ± 0.16

time steps, though this has a larger relative effect on the pressure work term. Presumably, an even smaller time step would further reduce this error.

As mentioned in section 3, the model is run using pressure averaging, which is used to smooth P and stabilize the model. To calculate the pressure work diagnostic $\mathbf{u} \cdot \nabla P$, \mathbf{u} is evaluated at single instant in time t_1 , but ∇P represents an average of three values at t_0 , $t_{0.5}$, and t_1 . The discrepancy between the precise instant in time at which the various quantities are sampled induces an error in the calculation. If the time step is smaller, the discrepancy between t_0 , $t_{0.5}$, and t_1 is smaller, and the error is reduced. If all the fields involved are slowly varying, this error is small, but the pressure work term is noisy even in the control run. This noisiness is exacerbated substantially by the addition of high-frequency forcing, as both ∇P and \mathbf{u} have more variability at high frequencies as ξ increases, and so the pressure work shows the largest changes when the temporal resolution is altered. The bottom drag has a similar issue: velocities at both t_0 and $t_{0.5}$ are used to calculate bottom drag, and as the near-inertial forcing increases, bottom drag changes with temporal resolution as well.

Using the low-passed velocities virtually eliminates the discrepancies in the velocities used to calculate the diagnostics and eliminates this source of error in the balanced budgets. Similarly, the advective sink is unaffected, as all velocities used to calculate it are at the same point in time.

APPENDIX B

2D FFT in Spherical Section

Because our model uses spherical coordinates, it is unclear how best to bin data in Fourier space. A 2D FFT

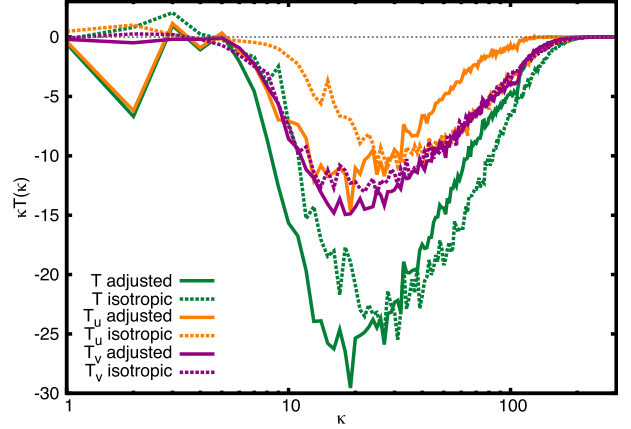


FIG. B1. Two ways of calculating the two-dimensional FFT. Solid lines use the adjusted scheme, and dashed lines use the isotropic scheme. Green lines show the total transfer, orange lines show the zonal contribution $T_u(\kappa)$, and purple lines show the meridional contributions $T_v(\kappa)$. Note that the peaks for $T_u(\kappa)$ and $T_v(\kappa)$ are aligned and slightly deeper in the adjusted scheme, while the peaks span a wider range of wavenumbers in the isotropic scheme.

of data on the latitude–longitude grid does not account for the convergence of meridians. To improve the accuracy of the 2D FFT, we split the calculation into parts and adjust the data to account for the curvature of the domain. Since the domain is periodic only in the zonal direction, we mirror the data in the meridional direction for double periodicity; the zonal velocity has an even extension and the meridional velocity has an odd extension.

We first calculate a zonal 1D FFT at each latitude. Since $\kappa = 1$ has a different physical meaning at each latitude, we then remap the data to an expanded (k_x, y) grid that can, at all latitudes, encompass both the largest and smallest physical wavelengths found in the domain. The largest and smallest wavelengths of the zonal modes are found at the northern (equatorward) and southern edges of the domain, respectively, and this gives the range of k_x needed for the expanded grid. Our adjusted scheme uses 1100 zonal bins, and the wavelengths resolved range from 4840 to 4.42 km. We remap the partially transformed data at each latitude to the new grid, rectifying the zonal grid in terms of physical wavelength (rather than numerical wavenumber). We do not smear the data or interpolate between bins to fill the gaps; we just space the data differently, leaving empty bins where appropriate. The few empty bins do not contribute to this second FFT, as an empty bin indicates that there is no energy at a specific combination of (physical) zonal and meridional wavelengths at the given latitude. The presence of empty bins does not substantially impact the resulting spectra. No adjustment is made meridionally since the meridional grid is evenly spaced. The 1D

meridional FFT is then performed along each adjusted k_x . Data are then binned in rings to calculate a one-dimensional transfer spectrum.

Figure B1 compares transfer spectra for the advective sink calculated using the reorganizing technique with the same spectra calculated using latitude–longitude binning for a representative member of our $\tau_0 = 0.15 \text{ Nm}^{-2}$ and $\xi = 0.5$ ensemble. Results are also decomposed into zonal and meridional contributions, that is,

$$\begin{aligned} T_u &= u^<[(\mathbf{v}^> \cdot \nabla)u^>]^<, \\ T_v &= v^<[(\mathbf{v}^> \cdot \nabla)v^>]^<, \quad \text{and} \\ T &= T_u + T_v = \mathbf{u}^< \cdot [(\mathbf{v}^> \cdot \nabla)\mathbf{u}^>]^<. \end{aligned}$$

Both sets of spectra have been normalized by the number of points in their respective grid.

The structures are broadly similar: both techniques generate spectra showing sinks of balanced energy at midrange wavenumbers, and the magnitude of the sink is comparable between the two calculations. But by splitting $T(\kappa)$ into its two constituent parts, we see that they have different shapes and that the adjusted scheme has a stronger effect on T_u than on T_v . The term T_v is distinctly larger and the peak value is around $\kappa = 18$ for both schemes. For T_u , the sink is significantly smaller than for T_v , and the peak wavenumber shifts from $\kappa \sim 32$ to $\kappa \sim 20$ between the two schemes. A net effect is that the adjusted scheme aligns the two contributions to the transfer spectrum. Note also that noisiness of the spectra here compared to those of Fig. 5 gives an indication of the variance within our ensembles.

REFERENCES

- Abernathy, R., J. Marshall, and D. Ferreira, 2011: The dependence of Southern Ocean meridional overturning on wind stress. *J. Phys. Oceanogr.*, **41**, 2261–2278, doi:10.1175/JPO-D-11-023.1.
- Alford, M. H., 2001: Internal swell generation: The spatial distribution of energy flux from the wind to the mixed layer near-inertial motions. *J. Phys. Oceanogr.*, **31**, 2359–2368, doi:10.1175/1520-0485(2001)031<2359:ISGTS>2.0.CO;2.
- , 2003a: Improved global maps and 54-year history of wind-work on the ocean inertial motions. *Geophys. Res. Lett.*, **30**, 1424, doi:10.1029/2002GL016614.
- , 2003b: Redistribution of energy available for ocean mixing by long-range propagation of internal waves. *Nature*, **423**, 159–162, doi:10.1038/nature01628.
- Bartello, P., 1995: Geostrophic adjustment and inverse cascades in rotating stratified turbulence. *J. Atmos. Sci.*, **52**, 4410–4428, doi:10.1175/1520-0469(1995)052<4410:GAAICI>2.0.CO;2.
- Bühler, O., 2003: Equatorward propagation of inertia–gravity waves due to steady and intermittent wave sources. *J. Atmos. Sci.*, **60**, 1410–1419, doi:10.1175/1520-0469(2003)060<1410:EPOIWD>2.0.CO;2.
- , and M. E. McIntyre, 2003: Remote recoil: A new wave–mean interaction effect. *J. Fluid Mech.*, **492**, 207–230, doi:10.1017/S0022112003005639.
- , and —, 2005: Wave capture and wave–vortex duality. *J. Fluid Mech.*, **534**, 67–95, doi:10.1017/S0022112005004374.
- Capet, X., J. McWilliams, M. Molemaker, and A. Shchepetkin, 2008: Mesoscale to submesoscale transition in the California Current System. Part I: Flow structure, eddy flux, and observational tests. *J. Phys. Oceanogr.*, **38**, 29–43, doi:10.1175/2007JPO3671.1.
- Danioux, E., J. Vanneste, P. Klein, and H. Sasaki, 2012: Spontaneous inertia–gravity-wave generation by surface-intensified turbulence. *J. Fluid Mech.*, **699**, 153–173, doi:10.1017/jfm.2012.90.
- Dong, S., J. Sprintall, S. T. Gille, and L. Talley, 2008: Southern Ocean mixed-layer depth from Argo float profiles. *J. Geophys. Res.*, **113**, C06013, doi:10.1029/2006JC004051.
- Fox-Kemper, B., R. Ferrari, and R. Hallberg, 2008: Parameterization of mixed layer eddies. Part I: Theory and diagnosis. *J. Phys. Oceanogr.*, **38**, 1145–1165, doi:10.1175/2007JPO3792.1.
- Furuichi, N., T. Hibiya, and Y. Niwa, 2008: Model-predicted distribution of wind-induced internal wave energy in the world’s oceans. *J. Geophys. Res.*, **113**, C09034, doi:10.1029/2008JC004768.
- Garrett, C., 2001: What is the “near-inertial” band and why is it different from the rest of the internal wave spectrum. *J. Phys. Oceanogr.*, **31**, 962–971, doi:10.1175/1520-0485(2001)031<0962:WITNIB>2.0.CO;2.
- Gertz, A., and D. N. Straub, 2009: Near-inertial oscillations and the damping of midlatitude gyres: A modeling study. *J. Phys. Oceanogr.*, **39**, 2338–2350, doi:10.1175/2009JPO4058.1.
- Grisouard, N., and L. N. Thomas, 2015: Energy exchanges between density fronts and near-inertial waves reflecting off the ocean surface. *J. Phys. Oceanogr.*, doi:10.1175/JPO-D-15-0072.1, in press.
- Huang, R. X., W. Wang, and L. L. Liu, 2006: Decadal variability of wind-energy input to the World Ocean. *Deep-Sea Res. II*, **53**, 31–41, doi:10.1016/j.dsr2.2005.11.001.
- Jiang, J., Y. Lu, and W. Perrie, 2005: Estimating the energy flux from the wind to ocean inertial motions: The sensitivity to surface wind fields. *Geophys. Res. Lett.*, **32**, L15610, doi:10.1029/2005GL023289.
- Josey, S. A., E. C. Kent, and P. K. Taylor, 2002: Wind stress forcing of the ocean in the SOC climatology: Comparisons with the NCEP–NCAR, ECMWF, UWM/COADS, and Hellerman and Rosenstein datasets. *J. Phys. Oceanogr.*, **32**, 1993–2019, doi:10.1175/1520-0485(2002)032<1993:WSFOTO>2.0.CO;2.
- Klein, P., and G. Lapeyre, 2009: The oceanic vertical pump induced by mesoscale and submesoscale turbulence. *Annu. Rev. Mar. Sci.*, **1**, 351–375, doi:10.1146/annurev.marine.010908.163704.
- Large, W., J. McWilliams, and S. Doney, 1994: Oceanic vertical mixing: A review and a model with a nonlocal boundary layer parameterization. *Rev. Geophys.*, **32**, 363–403, doi:10.1029/94RG01872.
- Levitus, S., and G. Isayev, 1992: Polynomial approximation to the international equation of state for seawater. *J. Atmos. Oceanic Technol.*, **9**, 705–708, doi:10.1175/1520-0426(1992)009<0705:PATTIE>2.0.CO;2.
- McDougall, T. J., D. R. Jackett, D. G. Wright, and R. Feistel, 2003: Accurate and computationally efficient algorithms for potential temperature and density of seawater. *J. Atmos. Oceanic Technol.*, **20**, 730–741, doi:10.1175/1520-0426(2003)20<730:AAEAF>2.0.CO;2.

- Molemaker, M. J., and J. C. McWilliams, 2010: Local balance and cross-scale flux of available potential energy. *J. Fluid Mech.*, **645**, 295–314, doi:[10.1017/S0022112009992643](https://doi.org/10.1017/S0022112009992643).
- , —, and I. Yavneh, 2005: Baroclinic instability and loss of balance. *J. Phys. Oceanogr.*, **35**, 1505–1517, doi:[10.1175/JPO2770.1](https://doi.org/10.1175/JPO2770.1).
- Ngan, K., D. Straub, and P. Bartello, 2004: Three-dimensionalization of freely-decaying two-dimensional turbulence. *Phys. Fluids*, **16**, 2918–2932, doi:[10.1063/1.1763191](https://doi.org/10.1063/1.1763191).
- , P. Bartello, and D. Straub, 2008: Dissipation of synoptic-scale flow by small-scale turbulence. *J. Atmos. Sci.*, **65**, 766–791, doi:[10.1175/2007JAS2265.1](https://doi.org/10.1175/2007JAS2265.1).
- Nikurashin, M., G. K. Vallis, and A. Adcroft, 2012: Routes to energy dissipation for geostrophic flows in the Southern Ocean. *Nat. Geosci.*, **6**, 48–51, doi:[10.1038/ngeo1657](https://doi.org/10.1038/ngeo1657).
- Rimac, A., 2014: The role of wind induced near-inertial waves on the energetics of the ocean. Ph.D. thesis, Max-Planck-Institut für Meteorologie, 124 pp.
- , J.-S. von Storch, C. Eden, and H. Haak, 2013: The influence of high-resolution wind stress fields on the power input to near-inertial motions in the ocean. *Geophys. Res. Lett.*, **40**, 4882–4886, doi:[10.1002/grl.50929](https://doi.org/10.1002/grl.50929).
- Scott, R. B., and Y. Xu, 2009: An update on the wind power input to the surface geostrophic flow of the World Ocean. *Deep-Sea Res. I*, **56**, 295–304, doi:[10.1016/j.dsr.2008.09.010](https://doi.org/10.1016/j.dsr.2008.09.010).
- Soward, A., and P. Roberts, 2010: The hybrid Euler–Lagrange procedure using an extension of Moffatt’s method. *J. Fluid Mech.*, **661**, 45–72, doi:[10.1017/S0022112010002867](https://doi.org/10.1017/S0022112010002867).
- Vanneste, J., 2008: Exponential smallness of inertia–gravity wave generation at small Rossby number. *J. Atmos. Sci.*, **65**, 1622–1637, doi:[10.1175/2007JAS2494.1](https://doi.org/10.1175/2007JAS2494.1).
- , 2013: Balance and spontaneous wave generation in geophysical flows. *Annu. Rev. Fluid Mech.*, **45**, 147–172, doi:[10.1146/annurev-fluid-011212-140730](https://doi.org/10.1146/annurev-fluid-011212-140730).
- Watanabe, M., and T. Hibiya, 2002: Global estimates of the wind-induced energy flux to inertial motions in the surface mixed layer. *Geophys. Res. Lett.*, **29**, 1239, doi:[10.1029/2001GL014422](https://doi.org/10.1029/2001GL014422).
- Whitt, D. B., and L. N. Thomas, 2015: Resonant generation and energetics of wind-forced near-inertial motions in a geostrophic flow. *J. Phys. Oceanogr.*, **45**, 181–208, doi:[10.1175/JPO-D-14-0168.1](https://doi.org/10.1175/JPO-D-14-0168.1).
- Williams, P. D., T. W. N. Haine, and P. L. Read, 2008: Inertia-gravity waves emitted from balanced flow: Observations, properties, and consequences. *J. Atmos. Sci.*, **65**, 3543–3558, doi:[10.1175/2008JAS2480.1](https://doi.org/10.1175/2008JAS2480.1).
- Wunsch, C., 1998: The work done by the wind on the oceanic general circulation. *J. Phys. Oceanogr.*, **28**, 2332–2340, doi:[10.1175/1520-0485\(1998\)028<2332:TWDBTW>2.0.CO;2](https://doi.org/10.1175/1520-0485(1998)028<2332:TWDBTW>2.0.CO;2).
- Xie, J.-H., and J. Vanneste, 2015: A generalised-Lagrangian-mean model of the interactions between near-inertial waves and mean flow. *J. Fluid Mech.*, **774**, 143–169, doi:[10.1017/jfm.2015.251](https://doi.org/10.1017/jfm.2015.251).
- Young, W., and M. Ben Jelloul, 1997: Propagation of near-inertial oscillations through a geostrophic flow. *J. Mar. Res.*, **55**, 735–766, doi:[10.1357/0022240973224283](https://doi.org/10.1357/0022240973224283).
- Zeitlin, V., 2008: Decoupling of balanced and unbalanced motions and inertia–gravity wave emission: Small versus large Rossby numbers. *J. Atmos. Sci.*, **65**, 3528–3542, doi:[10.1175/2008JAS2481.1](https://doi.org/10.1175/2008JAS2481.1).
- Zhai, X., R. J. Greatbatch, and J. Zhao, 2005: Enhanced vertical propagation of storm-induced near-inertial energy in an eddy-ocean channel model. *Geophys. Res. Lett.*, **32**, L18602, doi:[10.1029/2005GL023643](https://doi.org/10.1029/2005GL023643).
- , H. L. Johnson, D. P. Marshall, and C. Wunsch, 2012: On the wind power input to the ocean general circulation. *J. Phys. Oceanogr.*, **42**, 1357–1365, doi:[10.1175/JPO-D-12-09.1](https://doi.org/10.1175/JPO-D-12-09.1).